Soft Matter

Cite this: *Soft Matter*, 2012, **8**, 4109

www.rsc.org/softmatter

PAPER

Semidilute solutions of ultra-soft colloids under shear flow†

Dmitry A. Fedosov,[a] Sunil P. Singh,[a] Apratim Chatterji,[ab] Roland G. Winkler[a] and Gerhard Gompper*[a]

Received 20th October 2011, Accepted 5th January 2012
DOI: 10.1039/c2sm07009j

We study semidilute star-polymer solutions under shear flow by hybrid mesoscale simulations. Hydrodynamic interactions are modeled by two particle-based simulation techniques, multiparticle collision dynamics (MPC) and dissipative particle dynamics (DPD). Star polymers are considered as a paradigmatic model for ultra-soft colloids with variable softness. The influence of concentration and shear rate on their structural and rheological properties is investigated. Under flow, a star polymer elongates and displays a well-defined alignment angle with respect to the flow direction. Moreover, the structural and rheological properties exhibit a universal behavior as a function of a concentration-dependent Weissenberg number for various concentrations at a given arm length. The rheological properties are characterized by the shear viscosity and the normal-stress coefficients. In dilute solution, the zero-shear viscosity follows the Einstein relation with an effective radius given by the hydrodynamic radius of a star polymer. At high shear rates, the solutions exhibit shear-thinning behavior, where the viscosity decreases faster with increasing shear rate at higher concentrations. We demonstrate that the results obtained from MPC and DPD agree in all scaling properties, with minor quantitative deviations in the numerical values.

1 Introduction

The flow properties of solutions of macromolecules and colloids are of enormous importance for the behavior of many complex fluids, ranging from motor oils and drilling fluids to blood and the cytosol of living cells.[1] In many colloidal dispersions, the suspended particles are solid, but a much larger class of complex fluids contains deformable particles such as flexible synthetic polymers, semiflexible biopolymers, droplets, vesicles, capsules, and cells.

Linear and star polymers are particularly interesting model systems, because their size and architecture can be tailored in many different ways.[2] Studies of such systems are essential to obtain a detailed understanding of the rheological properties of complex fluids containing soft particles, which is required to design and control the flow behavior of fluids in technological or medical applications.

Star polymers consist of f identical linear polymer chains, which are linked at one of their ends to a common center. Each polymer arm contains N_m segments. By changing the arm length $L = N_m l$, where l is the bond length, and the functionality f, star-polymer properties can be varied between linear polymers (for $f = 2$) to nearly hard-sphere colloids (large functionality, short arms) and ultra-soft colloids (intermediate functionality, long arms).[2–5]

The equilibrium properties of star polymers have been studied in considerable detail.[3,5–8] The architecture of star polymers implies that the monomer density is high in the core region and decreases toward the corona. A consequence of this architecture and of the inhomogeneous density distribution is that the interaction is ultra-soft for sufficiently long chains, with a logarithmic dependence on the distance between two stars.[3–5] The ultra-soft interaction gives rise to an unusual phase diagram, for example with body-centered cubic (bcc) phases, which are not stable in systems of hard spheres,[9–12] reentrant melting,[5,13] and fcc-to-bcc transitions.[5,10,14]

Much less is known about the dynamical and rheological behavior of star-polymer solutions. Experiments show that self-diffusion decreases with increasing polymer concentration c according to a power law.[2,15] The diffusion coefficient of a star polymer in solution is larger than the diffusion coefficient of a hard-sphere colloid at equivalent volume fractions (defined by the hydrodynamic radius R_h in the case of star polymers). This is a direct consequence of the deformability and ultra-soft interactions of star polymers, which allow them to squeeze through gaps between other particles more easily. The same mechanism is responsible for the slower increase of the zero-shear viscosity with concentration for soft compared to hard particles.[2,15] In particular, it is observed that the viscosity of star-polymer solutions is finite even above the overlap concentration.[15,16] In

[a]*Theoretical Soft Matter and Biophysics, Institute of Complex Systems and Institute for Advanced Simulation, Forschungszentrum Jülich, 52425, Jülich, Germany. E-mail: g.gompper@fz-juelich.de*
[b]*Indian Institute of Science Education and Research (IISER), Pune, 411021, India*

† Electronic Supplementary Information (ESI) available: Two movies show simulation animations of semidilute star-polymer solutions for different shear rates. See DOI: 10.1039/c2sm07009j/

a related system of single DNA-grafted colloids, a strong dependence of the effective hydrodynamic radius on the conformation of the grafted polymer chains has been found.[17]

Theory and simulations have focused on the shape, orientation, and rotation of individual stars in shear flow,[18,19] on the dynamical frictional interactions between two stars[20] (both by an explicit bead-spring model of polymer chains), and on the rheology of concentrated solutions[21,22] (by a coarse-grained description with transient forces[23] between star centers).

The aim of the present study is to bridge the gap between the configurational and dynamical properties of individual star polymers, their hydrodynamic and steric interactions and the macroscopic flow behavior of semidilute solutions. So far, such systems have not been studied by simulations. Our investigations will help to establish a relation between the molecular architecture and microscopic deformation of individual soft colloids, and the macroscopic rheological behavior. Computer simulations of *linear* polymers in semidilute solutions show large deformations and a strong alignment of polymers along the flow direction in simple shear flow.[24,25] More importantly, in the stationary state, the *conformational* and *rheological properties* for various concentrations are universal functions of the Weissenberg number $Wi_c = \dot{\gamma}\tau(c)$, where $\dot{\gamma}$ is the shear rate and $\tau(c)$ the concentration-dependent polymer end-to-end vector relaxation time at equilibrium. Hence, with decreasing concentration, hydrodynamic interactions affect the conformational and rheological properties only by decreasing relaxation time $\tau(c)$. Experiments on DNA in shear flow[26] and simulations of polymer brushes[27] lead to a similar conclusion. We investigate here whether ultra-soft colloids in solution display a similar universal behavior in shear flow.

We use a standard bead–spring model to construct a polymer star. In order to account for hydrodynamic interactions, we employ two particle-based mesoscale simulation techniques, multiparticle collision dynamics (MPC)[28–30] and dissipative particle dynamics (DPD),[31,32] which are introduced in Sec. 2. This serves two purposes. On the one hand, we want to elucidate to what extend the two methods provide quantitatively equivalent results, and thereby test the suitability of these methods for predicting the non-equilibrium behavior of complex fluids; on the other hand, we want to establish method-independently the flow properties of ultra-soft colloids.

We will present and discuss in Sec. 3 several structural properties of star polymers in solutions under shear flow—such as the radius-of-gyration tensor and the alignment angle—as well as the corresponding bulk rheological properties of these solutions—such as shear-dependent viscosity and normal-stress coefficients. Finally, the results obtained by the two simulation techniques are compared with each other and with available experimental data in Sec. 4.

2 Methods and models

To model star-polymer solutions we employ two different mesoscopic simulation techniques: (i) multiparticle collision dynamics (MPC), also called stochastic rotation dynamics (SRD),[29,30] and (ii) dissipative particle dynamics (DPD).[31,32] Both methods implement proper hydrodynamic interactions and have been used in simulations of various soft matter and biological systems.[30,33]

2.1 Star-polymer model

We consider N_{sp} star polymers, where each star consists of f flexible linear polymer arms with one of their ends attached to a common center, which is illustrated in Fig. 1. Consecutive monomers of a polymer chain (arm) are connected by harmonic springs with the potentials

$$V_b = \frac{k_s}{2}(R_{i,i+1} - l)^2, \tag{1}$$

where $\boldsymbol{R}_{i,\,i+1} = \boldsymbol{R}_{i+1} - \boldsymbol{R}_i$ is the bond vector, $R_{i,\,i+1} = |\boldsymbol{R}_{i,\,i+1}|$, and l is the equilibrium bond length. The spring constant k_s is chosen such that even under strong shear stress the change in the equilibrium bond length remains less than a few percent. Excluded volume interactions between star monomers are implemented through the repulsive (truncated and shifted) Lennard-Jones (LJ) potential[34]

$$V_{LJ}(r) = 4\varepsilon\left[\left(\frac{\sigma}{r}\right)^{12} - \left(\frac{\sigma}{r}\right)^{6} + \frac{1}{4}\right]\Theta(2^{1/6} - r), \tag{2}$$

where $\Theta(r)$ is the Heaviside step function ($\Theta(r) = 0$ for $r < 0$ and $\Theta(r) = 1$ for $r \geq 0$). Since many polymer arms are attached to the center particle, the equilibrium bond length l_c of each center-arm connection and the LJ diameter σ_c of the central bead are taken to be twice as large as those for a normal monomer. We employ l as the unit of length, $\varepsilon = k_BT$ as the unit of energy, and m_s, the solvent particle mass, as the unit of mass. The unit of time is defined as $\tau = \sqrt{m_s l^2/(k_BT)}$. The parameters for star polymers for both MPC and DPD are listed in Table 1. The velocity Verlet algorithm is used to integrate Newtons' equations of motion of the star polymers with time step $h_m = 5 \times 10^{-3}\tau$ in MPC and $h_m = 8 \times 10^{-3}\tau$ in DPD.

2.2 Multiparticle collision dynamics

In the MPC algorithm, the solvent is modeled by N_s point particles with positions $\boldsymbol{r}_i$ and velocities $\boldsymbol{v}_i$ ($i = 1, \ldots, N_s$). The dynamics of these particles proceeds in discrete time increments

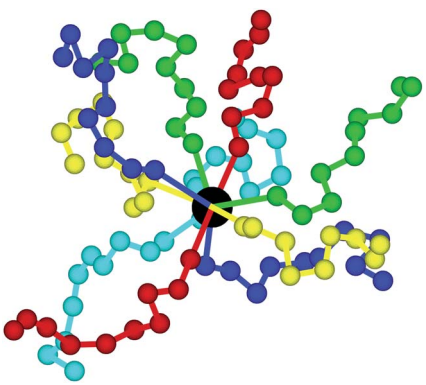

Fig. 1 A star polymer represented by a bead–spring model with $f = 10$ linear-polymer arms, connected to a common central (black sphere). The length of each arm is $N_m = 10$. The arms are colored for better visual differentiation.

Table 1 Star-polymer parameters in MPC and DPD simulations, where subscripts '*m*' and '*c*' denote arm monomers and central bead, respectively

	$k_s l^2/k_B T$	l_c/l	σ_m/l	σ_c/l	M_m/m_s	M_c/m_s
MPC	1000	2.0	0.8	1.6	10	10
DPD	125	2.0	0.8	1.6	2	10

h, denoted as collision time, by alternating streaming and collision steps.[29,30] In the streaming step, the solvent particles of mass m_s move ballistically with their respective velocities, and their positions are updated as

$$\boldsymbol{r}_i(t+h) = \boldsymbol{r}_i(t) + h\boldsymbol{v}_i(t). \tag{3}$$

After each streaming step, solvent particles are sorted into the cells of a simple cubic lattice with lattice constant a. Their relative velocities, with respect to the center-of-mass velocity of the cell, are rotated around a randomly oriented axis by an angle α, so that

$$\boldsymbol{v}_i(t+h) = \boldsymbol{v}_i(t) + (\mathbf{R}(\alpha) - \mathbf{I})(\boldsymbol{v}_i(t) - \boldsymbol{v}_{cm}(t)), \tag{4}$$

where $\mathbf{R}$ is the rotation matrix, $\mathbf{I}$ is the unit matrix, and $\boldsymbol{v}_{cm} = \frac{1}{N_c}\sum_{j=1}^{N_c}\boldsymbol{v}_j$ is the center-of-mass velocity of the cell with N_c particles. The collision step is a stochastic process, where mass, energy, and momentum are conserved, which ensures that hydrodynamic behavior emerges on larger length scales.

The star polymers are coupled to the solvent during the collision step, where their monomers are included in the collisions together with the solvent particles.[35,36] Thereby, momentum is redistributed between solvent and monomers in the same cell.

Transport properties of the solvent depend on the collision time h, the rotation angle α, and the average number density per cell. Tuning these variables allows us to attain solvents with a high Schmidt number, where momentum transport dominates over mass transport. Some of the simulation parameters for MPC system are summarized in Table 2. These parameters correspond to the solvent viscosity $\eta_s = 8.7\sqrt{m_s\varepsilon/l^4}$ and the Schmidt number $Sc \approx 17$.

Lees–Edwards boundary conditions are applied for the solvent particles and the monomers in order to impose shear flow.[37] This yields a linear fluid velocity profile $v_x = \dot{\gamma}y$ in the flow direction (x-axis) as a function of their position along the gradient direction (y-axis), where $\dot{\gamma}$ is the shear rate. A local cell-wise Maxwellian thermostat is applied to maintain the desired temperature of the fluid.[38]

2.3 Dissipative particle dynamics

Similar to MPC, a DPD system consists of a collection of N_s point particles. DPD particles interact through simple pairwise-additive forces corresponding to a conservative force F_{ij}^C, a dissipative force F_{ij}^D, and a random force F_{ij}^R. The total force exerted on a particle i by particle j consists of the three terms given by

$$\begin{aligned}
\boldsymbol{F}_{ij}^C &= b\left(1 - \frac{r_{ij}}{r_C}\right)\hat{\boldsymbol{r}}_{ij},\\
\boldsymbol{F}_{ij}^D &= -\gamma\omega^D(r_{ij})(\boldsymbol{v}_{ij}\cdot\hat{\boldsymbol{r}}_{ij})\hat{\boldsymbol{r}}_{ij},\\
\boldsymbol{F}_{ij}^R &= \sigma_{ran}\omega^R(r_{ij})\frac{\xi_{ij}}{\sqrt{h}}\hat{\boldsymbol{r}}_{ij},
\end{aligned} \tag{5}$$

where $\boldsymbol{r}_{ij} = \boldsymbol{r}_i - \boldsymbol{r}_j$, $\hat{\boldsymbol{r}}_{ij} = \boldsymbol{r}_{ij}/r_{ij}$, and $\boldsymbol{v}_{ij} = \boldsymbol{v}_i - \boldsymbol{v}_j$. The coefficients b, γ, and σ_{ran} determine the strength of conservative, dissipative, and random forces, respectively. ω^D and ω^R are weight functions and ξ_{ij} is a symmetric normally-distributed random variable with zero mean and unit variance. All forces act within a sphere of cutoff radius r_c. The random and dissipative forces must satisfy the fluctuation-dissipation theorem[32] in order for the DPD system to maintain the equilibrium temperature T, which is enforced through the two conditions $\omega^D(r_{ij}) = [\omega^R(r_{ij})]^2$ and $\sigma_{ran}^2 = 2\gamma k_B T$. The usual choice for the weight function is $\omega^R(r_{ij}) = (1 - r_{ij}/r_c)^p$, where $p = 1$ for the original DPD method. However, other choices (*e.g.*, $p = 0.25$) for these envelopes have been used[39,40] in order to increase the viscosity of the DPD fluid and bring the Schmidt number in DPD to values representative of real liquids. The time evolution of velocities and positions of particles is determined by Newton's second law of motion, which is integrated using the velocity–Verlet algorithm.

The simulation parameters for the DPD system are listed in Table 3. With these parameters, we obtain a Schmidt number $Sc = 1011$. The time step is set to $h = h_m = 8 \times 10^{-3}\tau$. Star polymers are constructed similarly to that described in Sec. 2.1 and are coupled to the fluid through DPD forces with $b_{ps}l/\varepsilon = 0$, $\gamma_{ps}\tau/m_s = 7.5$, and $p_{ps} = 0.25$, where the subscript ps denotes polymer–solvent interactions. Lees–Edwards boundary conditions are employed to model steady shear flow, as described above in Sec. 2.2.

3 Results and discussion

A list of parameters of star-polymer solutions for both mesoscale hydrodynamic simulation techniques is given in Table 4; it provides information about the size of simulation box $L_x \times L_y \times L_z$, the range of number of star polymers N_{sp}, and the ranges of simulated shear rates $\dot{\gamma}$ and concentrations c. All results are obtained for functionality $f = 10$, with arm lengths in the range $N_m = 10$–30. Specifically, MPC simulations are performed for $N_m = 10$ and 30, DPD simulations for $N_m = 10$ and 20. The simulations for $N_m = 10$ are performed with both MPC and DPD in order to compare the results and to show that the predictions for the properties of star-polymer solutions are independent of the

Table 2 MPC fluid parameters in the simulations. $\langle N_c\rangle$ is the average number of solvent particles per cell

a/l	α	$\langle N_c\rangle$	h/τ	$\eta_s/\sqrt{m_s k_B T/l^4}$
1.0	130°	10.0	0.1	8.7

Table 3 DPD fluid parameters in simulations. The subscript *ss* denotes the corresponding parameters for solvent–solvent interactions. n is the solvent number density

$b_{ss}l/\varepsilon$	$\gamma_{ss}\tau/m_s$	p_{ss}	r_c/l	nl^3	$\eta_s/\sqrt{m_s k_B T/l^4}$
20.0	5.0	0.15	3.0	0.375	8.21

Table 4 List of simulation parameters. L_x, L_y, and L_z denote the dimensions of the simulation box and $\dot{\gamma}$ is the shear rate. R_{g0} and R_h are the equilibrium radius of gyration and hydrodynamic radius in dilute solution, respectively, and τ_z is the Zimm relaxation time

Method	N_m	N_{sp}	$L_x/l \times L_y/l \times L_z/l$	R_{g0}/l	R_h/l	τ_z/τ	c/c^*	$\dot{\gamma}\tau$
MPC	10	20–200	$30 \times 30 \times 30$	3.54	3.74	870	0.17–1.65	10^{-5}–5×10^{-2}
MPC	30	100–750	$100 \times 100 \times 100$	7.14	7.10	7830	0.15–1.13	10^{-5}–2.5×10^{-2}
DPD	10	23–299	$50 \times 34 \times 36.2$	4.06	4.10	821	0.1–1.3	5×10^{-5}–1.6×10^{-2}
DPD	20	30–390	$76 \times 52 \times 51.8$	5.80	5.46	3285	0.1–1.3	5×10^{-5}–1.6×10^{-2}

employed method. In the other set of simulations with $N_m = 20$ in DPD and $N_m = 30$ in MPC, we intend to obtain the solution properties for a wider range of arm lengths N_m. We measure concentration relative to the overlap concentration

$$c^* = \left[\frac{4}{3}\pi R_h^3\right]^{-1} \tag{6}$$

where R_h is the hydrodynamic radius.

The applied shear flow is characterized by the dimensionless Weissenberg number $Wi = \dot{\gamma}\tau_z$, where $\tau_z = \eta_s N_m^2 l^3/k_B T$ is the Zimm relaxation time of a polymer arm in dilute solution. At low shear rates or small $Wi \ll 1$, star polymers are close to their equilibrium structure. However, at large $Wi \gg 1$, they are strongly deformed and aligned with the flow as shown by the snapshots in Fig. 2. The relaxation time of a star polymer increases with concentration, which suggests to use the concentration-dependent Weissenberg number $Wi_c = \beta\,(c/c^*)\,Wi$ to take this change into account. As has been shown recently for semi-dilute solutions of *linear polymers*, the concentration dependence of structural and rheological properties are captured very well in this way and universal curves are obtained.[24,25]

The lengths of typical simulation runs were at least several tens of times the equilibrium polymer relaxation time τ, and up to several hundred times τ for low shear rates.

3.1 Radius-of-gyration tensor

Two characteristic conformations of star polymers in solution at intermediate and high shear rates are shown in Fig. 2. To quantitatively characterize the effect of shear flow on the structural properties of star polymers we calculate the radius of gyration tensor of a star polymer according to

$$G_{\alpha\beta} = \frac{1}{N}\left\langle \sum_{i=1}^{N} \Delta r_i^{\alpha} \Delta r_j^{\beta} \right\rangle, \tag{7}$$

where $N = fN_m + 1$ is the total number of monomers in a star, Δr_i is the position of the i^{th} monomer relative to the star center of mass, and $\alpha, \beta \in \{x, y, z\}$. In equilibrium, all diagonal components of $G_{\alpha\beta}$ are equal, *i.e.*, $G_{\alpha\alpha} = G_{\alpha\alpha}^{00} = R_{g0}^2/3$, where R_{g0} is the radius of gyration. In the dilute regime, the radius of gyration follows the scaling relation $R_{g0}^2 \sim l_0^2 N_m^{2\nu} f^{1-\nu}$ in terms of arm length and functionality,[3,6–8] with the exponent $\nu \approx 0.63$ for our system.

Under shear flow, polymers along the flow direction become elongated; their relative deformation in this direction is calculated as

$$\delta G_{xx}(c/c^*) = \frac{G_{xx}(c/c^*) - G_{xx}^0(c/c^*)}{G_{xx}^0(c/c^*)}, \tag{8}$$

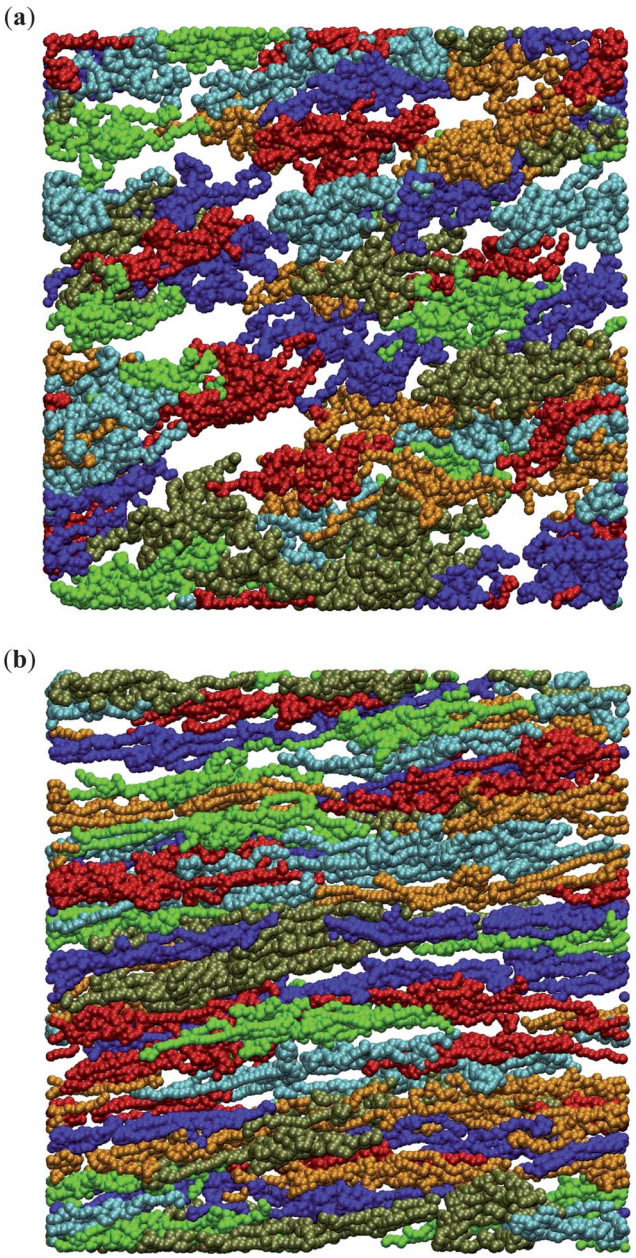

Fig. 2 Simulation snapshots of star-polymer solutions with functionality $f = 10$, arm length $N_m = 30$, and concentration $c/c^* = 0.75$ (where c^* is the overlap concentration, see Sec. 3). (a) Intermediate shear rate with concentration-dependent Weissenberg number $Wi_c = 15$, and (b) high shear rate with $Wi_c = 153$ (for definition of Wi_c see Sec. 3). Only star polymers with their centers in a slice of thickness of twice the radius of gyration R_{g0} parallel to the flow-gradient plane are shown. The multiple colors serve to make different star polymers easily distinguishable. Corresponding movies are shown in the ESI.†

where G^0_{xx} is the radius of gyration at equilibrium for a given concentration. A comparison of simulation data of δG_{xx} for various concentrations and arm lengths at the same Weissenberg number Wi shows that stars at higher concentrations exhibit a stronger stretching than those at lower c/c^*. This is due to differences in the relaxation times, which increase with increasing concentration.[24] We can estimate the concentration dependence of the relaxation time by scaling the Weissenberg number by a factor β (c/c^*), in order to shift δG_{xx} for high concentrations to the lowest concentration curve. A universal curve is then obtained for the relative deformation δG_{xx} as function of $Wi_c = \beta$ (c/c^*) Wi for the various polymer lengths and both simulation methods, as shown in Fig. 3. At large shear rates, the extension of star polymers saturates at a maximum value, which depends on the length of the polymer arms. At low $Wi_c < 1$, a quadratic dependence of the relative deformation (solid black line) as a function of shear rate is observed, which has also been seen in previous MPC simulations of single star polymers[18] and of semidilute solutions of linear polymers,[24] as well as in experiments.[41]

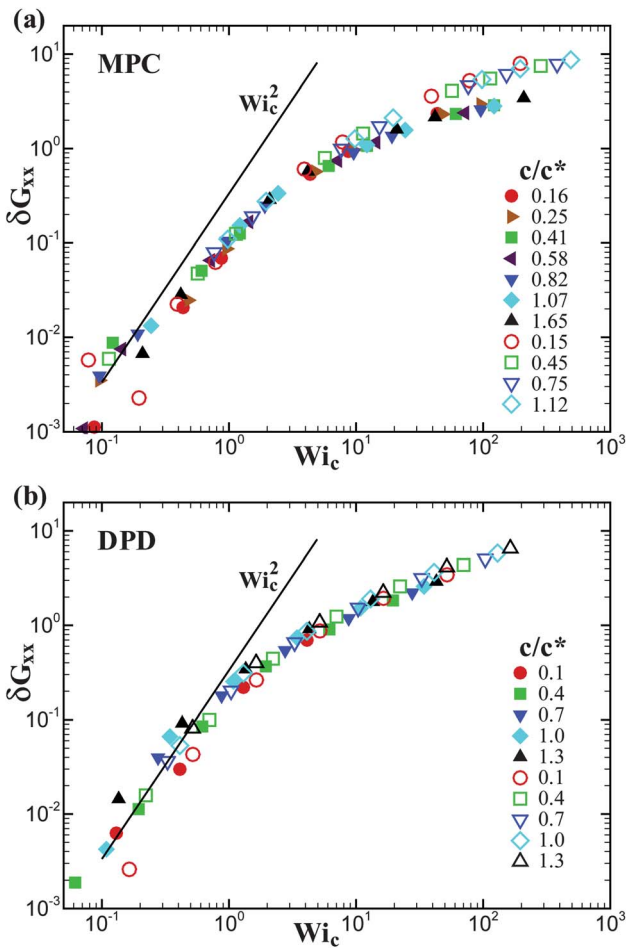

Fig. 3 Relative deformation δG_{xx} of star polymers along the flow direction as function of the concentration-dependent Weissenberg number Wi_c. (a) MPC simulation results, with arm lengths $N_m = 10$ (filled symbols) and $N_m = 30$ (open symbols), and various concentrations c/c^*, as indicated. (b) DPD simulation results for various star-polymer concentrations, as indicated, and $N_m = 10$ (filled symbols) and $N_m = 20$ (open symbols). The black solid lines indicate a quadratic dependence of the relative deformation on Wi_c at low shear rates; these lines are identical in (a) and (b).

The scale factors β (c/c^*) are displayed in Fig. 4 as a function of concentration. The values of β (c/c^*) from the MPC simulations for $N_m = 10$ and 30 and DPD simulations for $N_m = 10$ and 20 are nearly independent of arm length. In Fig. 3, the scaling of δG_{xx} with Wi_c and the functional dependence are in very good agreement for both methods; there is a small difference in the absolute values, which will be discussed in more detail in Sec. 4. Since the scale factor is proportional to the ratio of star relaxation times for different concentrations, the characteristic relaxation time on the star concentration appears to be nearly independent of the arm length.

Along the shear-gradient and vorticity directions, star polymers shrink at high Wi_c. Fig. 5 displays the scaled curves for the gyration tensor G_{yy}/G^{00}_{yy} as a function of Wi_c, where G^{00}_{yy} corresponds to the y component of the radius of gyration in equilibrium and in the dilute limit. The differences in the plateau values of G_{yy}/G^{00}_{yy} at low Wi_c are associated with the change in star-polymer size at various concentrations indicating that the stars become more compact due to their crowding. Compression in the vorticity direction is quite small in comparison with the gradient direction, consistent with previous results for single star polymers.[18]

3.2 Star-polymer alignment

Flow-induced alignment of star polymers can be characterized by the angle χ_G, which is the angle between the eigenvector of the gyration tensor with the largest eigenvalue and the flow direction. It can be computed from the components of the gyration tensor as

$$\tan(2\chi_G) = \frac{2G_{xy}}{G_{xx} - G_{yy}}. \quad (9)$$

Fig. 6 shows the alignment angle of star polymers as function of Wi_c for various concentrations and both simulation methods.

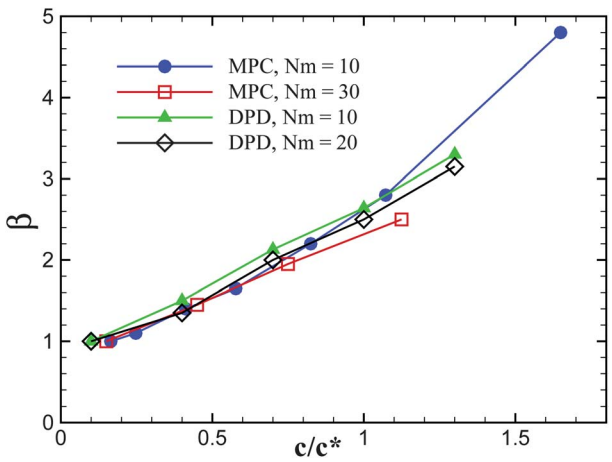

Fig. 4 Concentration-dependent scale factor for the relaxation time $(\tau(c) = \beta(c)\tau_z)$ obtained from the scaling of the radius-of-gyration tensor along the shear direction. MPC and DPD results are shown for various arm lengths N_m, as indicated.

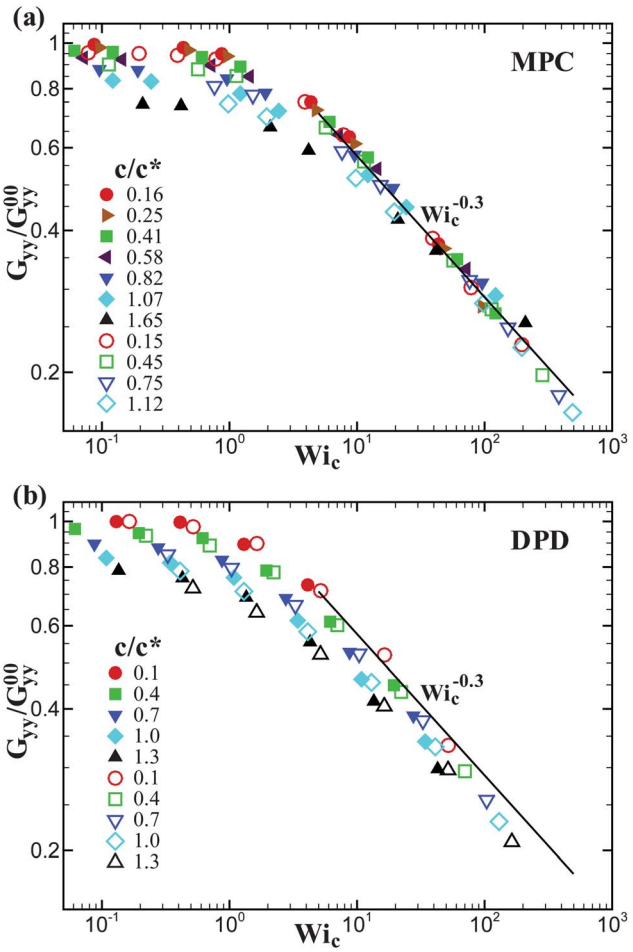

Fig. 5 Star-polymer deformation along the gradient direction, G_{yy}/G_{yy}^{00}, as function of Wi_c. (a) MPC simulation results, with arm lengths $N_m = 10$ (filled symbols) and $N_m = 30$ (open symbols), and various concentrations c/c^*, as indicated. (b) DPD simulation results for various star-polymer concentrations, as indicated, and $N_m = 10$ (filled symbols) and $N_m = 20$ (open symbols).

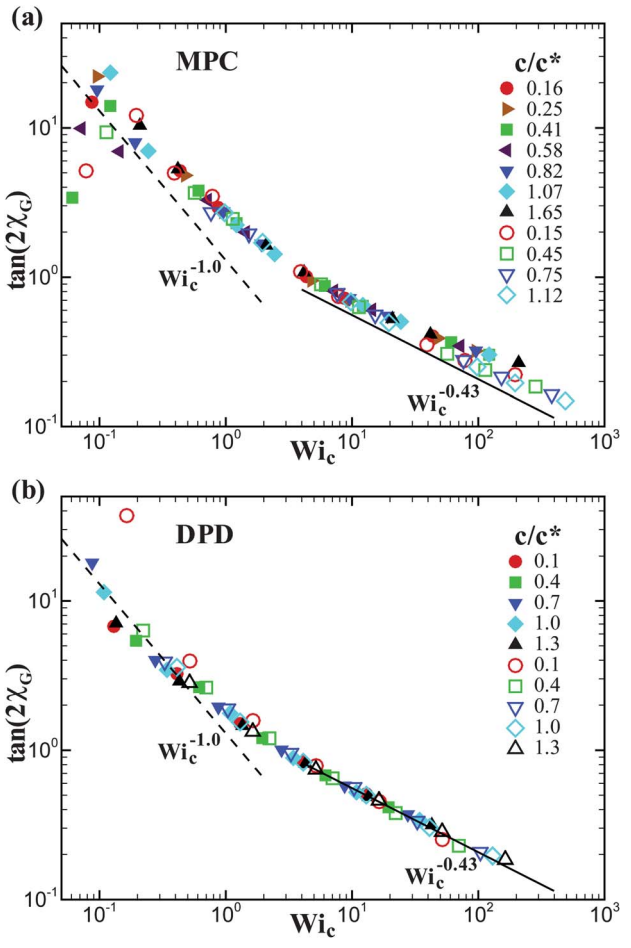

Fig. 6 Orientation of star polymers $\tan(2\chi_G)$ as function of Wi_c. (a) MPC simulation results, with arm lengths $N_m = 10$ (filled symbols) and $N_m = 30$ (open symbols), and various concentrations c/c^*, as indicated. (b) DPD simulation results for various star-polymer concentrations, as indicated, and $N_m = 10$ (filled symbols) and $N_m = 20$ (open symbols). The dashed black lines indicate a scaling behavior $\tan(2\chi_G) \sim Wi_c^{-1}$ and the solid black lines correspond to $\tan(2\chi_G) \sim Wi_c^{-0.43}$. Note that lines in (a) and (b) are identical.

At low shear rates the alignment angle χ_G is close to the equilibrium value $\pi/4$. For $0 < Wi_c < 1$, the data in Fig. 6(a) obey the expected scaling behavior[42,43] $\tan(2\chi_G) \sim Wi_c^{-1}$, which follows from the fact that $G_{xy} \sim Wi_c$ and $G_{xx} - G_{yy} \sim Wi_c^2$ in that regime. At high Wi_c, star polymers deform into an ellipsoidal shape, and the angle χ_G decreases due to alignment of the star along the flow direction. Again, a universal curve is obtained for different star-polymer concentrations and both MPC and DPD methods as a function of Wi_c. At high Wi_c, the alignment angle follows the scaling law

$$\tan(2\chi_G) \sim (Wi_c)^{-\delta} \tag{10}$$

with the exponent of $\delta \approx 0.43$. The master curve obtained for different arm lengths is almost independent of N_m for $Wi_c < 20$. At higher Wi_c, effects of finite arm length may play a role, as in systems of linear polymers.[24] Stars with longer arms appear to be more aligned with the flow direction than those with shorter arms at $Wi_c > 20$. This is due to the fact that the crossover from the behavior $\tan(2\chi_G) \sim Wi_c^{-1}$ to the asymptotic behavior $\tan(2\chi_G) \sim Wi_c^{-1/3}$, predicted by theory for linear polymers,[43] appears at smaller Wi_c for longer polymers.

The shear-induced structural deformation and alignment of star polymers can be visualized in terms of their monomer density distribution in the flow-gradient plane. In Fig. 7, such distributions of individual stars are presented for $Wi_c = 0.78$, 7.8, and 78. At very low shear rates, the stars are close to their equilibrium shape and the density distribution is spherically symmetric. An increase of the shear rate leads to the alignment of star polymers along the flow direction. For $Wi_c \gg 1$, star arms are highly stretched along the flow and compressed in the gradient direction. Particularly at high shear rates, the density distribution is not of elliptical but rather of rhombic shape, with nearly flat parts along the flow direction.

3.3 Rheology

To characterize the rheological properties of the star-polymer solutions, we determine various components of the stress tensor,

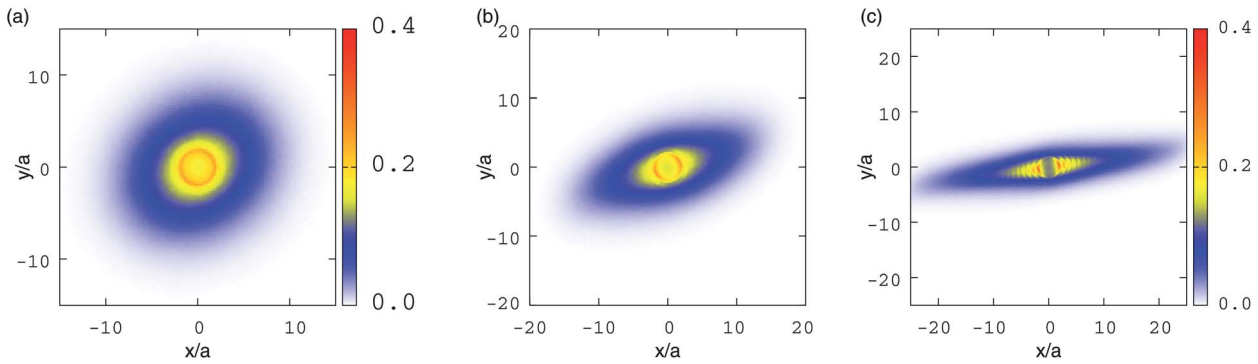

Fig. 7 Monomer density distributions of individual star polymers in the flow-gradient plane for various Weissenberg numbers, (a) $Wi_c = 0.78$, (b) $Wi_c = 7.8$, and (c) $Wi_c = 78.0$. The arm length is $N_m = 30$ and the polymer concentration is $c/c^* = 0.15$. The density distributions are indistinguishable between the two simulation approaches. The strip-like density modulations in (c) reflect the monomer-density modulations of the strongly stretched and aligned polymers.

in particular σ_{xy}, σ_{xx}, σ_{yy}, and σ_{zz}, using the Irving–Kirkwood formula for the virial.[44,45] We consider only the star-polymer contributions to the virial, which includes their bond and excluded-volume contributions. The shear viscosity as a function of shear rate follows from $\eta(\dot\gamma) = \sigma_{xy}(\dot\gamma)/\dot\gamma$. In addition, we compute the corresponding first and second normal-stress coefficients Ψ_1 and Ψ_2 defined as

$$\Psi_1(\dot\gamma) = \frac{\sigma_{xx}(\dot\gamma) - \sigma_{yy}(\dot\gamma)}{\dot\gamma^2}, \qquad \Psi_2(\dot\gamma) = \frac{\sigma_{yy}(\dot\gamma) - \sigma_{zz}(\dot\gamma)}{\dot\gamma^2}. \quad (11)$$

For many polymeric fluids, the viscosity function and normal-stress coefficients display zero-shear rate plateaus at low shear rates, which is often referred to as low-shear-rate Newtonian regime.

Fig. 8 shows shear stresses σ_{xy} normalized by σ^0_{xy} for different arm lengths and concentrations as a function of Wi_c. σ^0_{xy} follows from the relation $\sigma_{xy} = \sigma^0_{xy}\, Wi_c$ in the limit of small shear rates; its dependence on concentration is presented in Fig. 9.

Evidently, the shear stress is a linear function of shear rate for $Wi_c < 1$ independent of concentration. At larger Weissenberg numbers, a crossover can be observed to a weaker dependence on Wi_c. In that regime, we observe a non-universal concentration dependence; $\sigma_{xy}/\sigma^0_{xy}$ is larger at smaller concentrations, but the data seem to converge toward a common limiting behavior with increasing concentration. Both, MPC and DPD simulations exhibit the same behavior.

The dimensionless stress scale factors $\sigma^0_{xy} R_h^3/(k_B T)$ in Fig. 9 are virtually independent of the star-polymer arm length. This demonstrates that the characteristic relaxation time of a star polymer exhibits a similar length dependence as R_h^3. A slight deviation is found between the stress scale factors for MPC and DPD simulations. We attribute this deviation to differences in the way a star polymer is coupled to the solvent in the two approaches.

The viscosities of the star-polymer solutions are displayed in Fig. 10 for various arm lengths and concentrations. The curves are scaled by the corresponding zero-shear viscosity η_0 in order to verify and find a scaling behavior. The values of η_0 for the systems with $N_m = 10$ can directly be extracted from simulations. However, for the systems of longer chains, the zero-shear plateau appears only at extremely low shear rates, which is difficult to

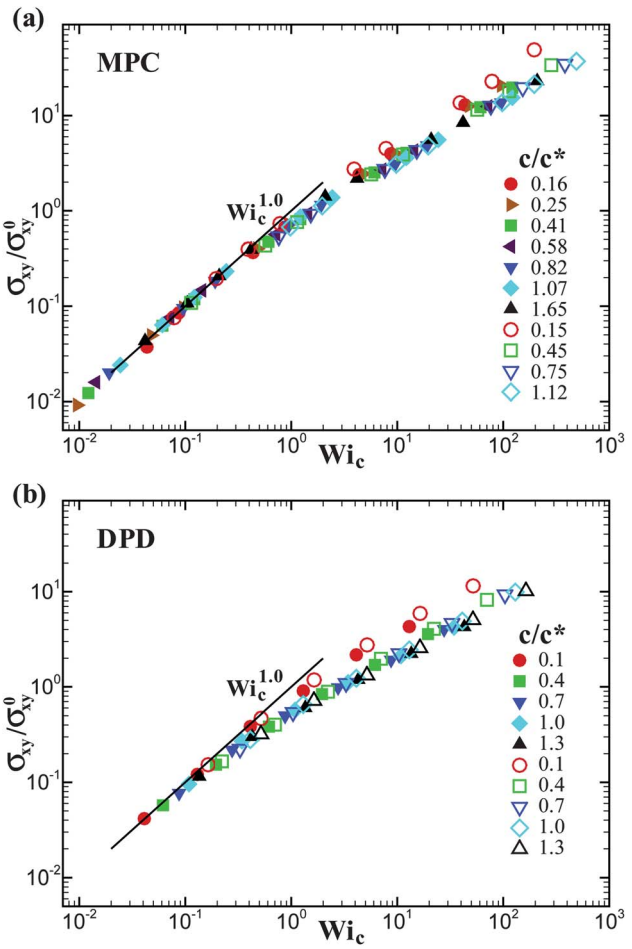

Fig. 8 Normalized shear stress $\sigma_{xy}/\sigma^0_{xy}$ of star-polymer solutions with respect to Wi_c, where $\sigma_{xy} = \sigma^0_{xy} Wi_c$ as $\dot\gamma \to 0$, see Fig. 9. (a) MPC simulation results, with arm lengths $N_m = 10$ (filled symbols) and $N_m = 30$ (open symbols), and various concentrations c/c^*, as indicated. (b) DPD simulation results for various star-polymer concentrations, as indicated, and $N_m = 10$ (filled symbols) and $N_m = 20$ (open symbols). Only polymer contributions to the virial are included.

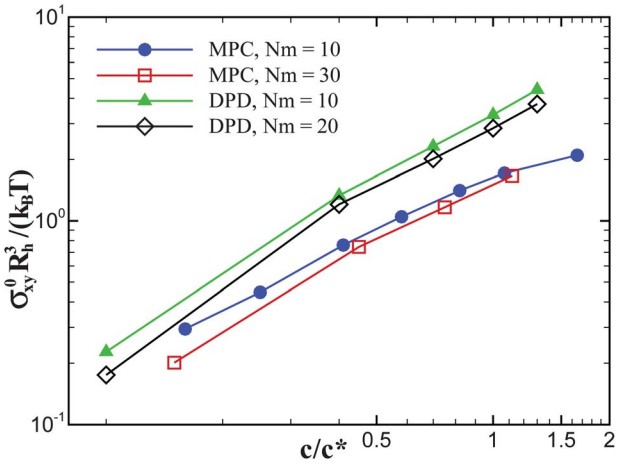

Fig. 9 Scaling factors σ^0_{xy} (normalized by k_BT/R_h^3) for the shear stress of star-polymer solutions at different concentrations. σ^0_{xy} values are computed as σ_{xy}/Wi_c at low shear rates ($\dot{\gamma} \to 0$).

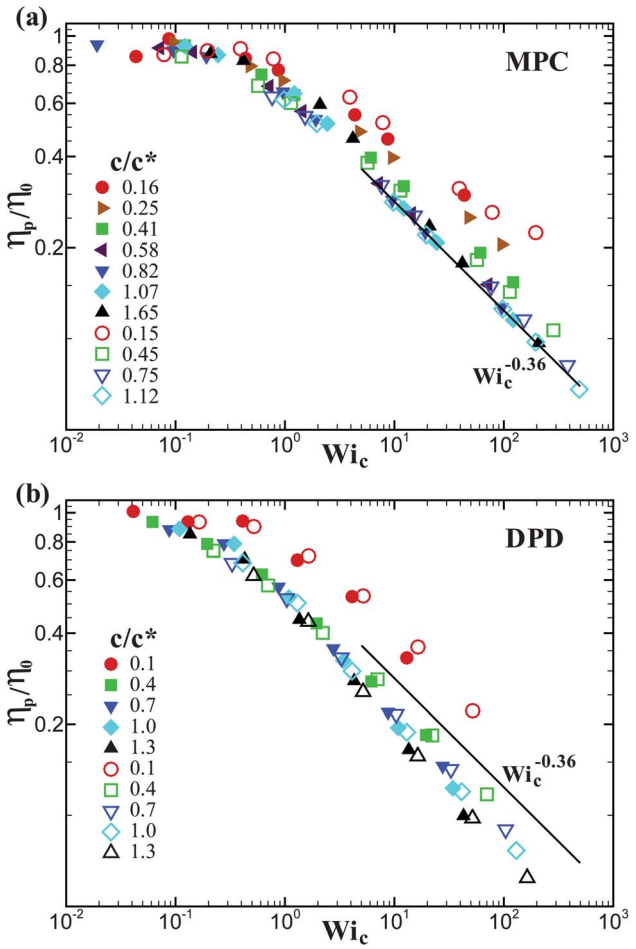

Fig. 10 Shear-rate-dependent viscosity of simulated star-polymer solutions for various arm lengths and concentrations as a function of Wi_c. (a) MPC simulation results, with arm lengths $N_m = 10$ (filled symbols) and $N_m = 30$ (open symbols), and various concentrations c/c^*, as indicated. (b) DPD simulation results for various star-polymer concentrations, as indicated, and $N_m = 10$ (filled symbols) and $N_m = 20$ (open symbols). Only polymer contributions to the viscosity are shown. The viscosity curves are scaled with the corresponding values of the zero-shear viscosity η_0 for different concentrations. The solid lines indicate the power-law dependence $\eta_p \sim Wi_c^{-0.36}$; they are identical in (a) and (b).

access in simulations, since thermal fluctuations overwhelm average flow properties and reliable statistics are difficult to obtain. An additional simulation complexity for star systems with long arms is related to the characteristic relaxation time of such stars, which becomes very long in comparison to that of the stars with relatively short arms and leads to demanding simulation times. Therefore, the various viscosity curves for $N_m = 20$ and 30 in Fig. 10 were scaled to match the lowest available concentration results at low shear rates, which may not necessarily be within the zero-shear plateau, but are likely within the transition region to the power-law regime.

At $Wi_c > 1$, the viscosities exhibit a power-law decay with increasing shear rate (Fig. 10). An interesting feature is that the power-law exponent appears to dependent on the star-polymer concentration, a dependence already visible for the shear stress in Fig. 8. At low concentrations, the exponent is equal to approximately -0.3, while at high star concentrations $c/c^* \simeq 1.3$ it is about -0.4. Such a dependence has not been predicted by any theory and appears to be independent of arm length, but is consistently obtained with both simulation techniques. The concentration dependence results in a poor scaling of the viscosity curves, suggesting that a common master curve for the shear viscosity behavior may not exist. This is in contrast to simulations results for linear polymers, where the viscosities hardly exhibit a concentration dependence when data are plotted as a function of Wi_c.[24] It is not evident what causes the differences in the behavior of linear and star polymers, keeping in mind that the stress tensor is in essence determined by the virial term of the polymer-bond contributions. We would like to point out, however that the star-polymer dynamics under flow is distinctly different from that of a linear polymer—a linear polymer undergoes tumbling motion,[25] whereas star polymers show a tank-treading-like rotation[18] for functionalities $f > 5$.

Fig. 11 presents the zero-shear viscosity values for various arm lengths with respect to star concentration extracted from the scaling of the polymer contribution η_p to the viscosity. For the star solutions with $N_m = 10$, in DPD simulations we have also used an alternative method, called reverse Poiseuille flow (RPF), in order to estimate the zero-shear viscosity.[46] The RPF is generated from two Poiseuille flows driven by uniform body forces in opposite directions along two halves of a periodic computational domain. The zero-shear viscosities computed with RPF are in excellent agreement with those values obtained by proper scaling of the viscosity curves as done in Fig. 10.

Evidently, the star-polymer concentrations exceed the linear regime, where $\eta_0/\eta_s = 2.5\phi$ applies as predicted by Einstein[47] for colloids of volume fraction ϕ—in our case $\phi = c/c^*$. The MPC data follow the dependence $\eta_0/\eta_s = 2.5\phi + 6.2\phi^2$ proposed for Brownian solutions.[48] The DPD simulations yield somewhat larger viscosity ratios η_0/η_s, but the dependence on c/c^* is very similar. In addition, the dependence $(1 - \phi/\phi_m)^{-2.5\phi_m}$ is plotted, which is valid for a colloidal solution.[49]

It is clear that there is only a weak dependence of the zero-shear viscosity on the arm length N_m. This is again an indication that certain properties of star-polymer solutions may be absorbed in the star hydrodynamic radius R_h, which determines the

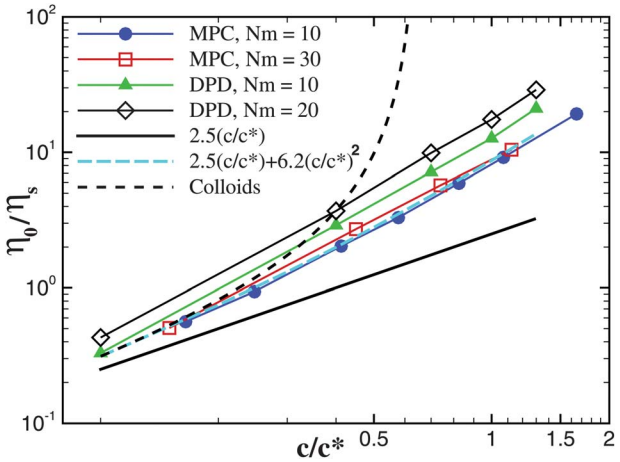

Fig. 11 Zero-shear viscosity normalized by η_s as a function of star-polymer concentration c/c^*, for various N_m as indicated. Several theoretical predictions for a colloidal solution are also plotted. The solid black line corresponds the linear regime $\eta_0/\eta_s = 2.5\phi$ predicted by Einstein[47] for colloids, where $\phi = c/c^*$. The cyan dashed curve displays the dependence of $\eta_0/\eta_s = 2.5\phi + 6.2\phi^2$ for Brownian solutions.[48] The black dashed curve indicates the dependence of $(1 - \phi/\phi_m)^{-2.5\phi_m}$, which is valid for a solution of colloids.[49]

solution concentration. In contrast to these results are experimental measurements of η_0 for star solutions with different functionalities,[15] which show a strong dependence of η_0 on f such that the star solution viscosity approaches the viscosity curve for a colloidal solution at high f. This is likely a consequence of the increasing monomer concentration around the star center, which is altered substantially for varying f. Thus, star functionality would be directly associated with star softness, while N_m effectively changes the size of a star polymer.

We have introduced three scale factors, β, σ^0_{xy}, and η_0, which are not independent. They are rather related and the ratio $\eta_0/(\sigma^0_{xy}\beta)$ is approximately constant.

Fig. 12 shows the normalized first normal-stress coefficient Ψ_1. The curves of Ψ_1 for various concentrations are scaled by factors ψ_1^0, which are displayed in Fig. 14. As expected, we find a plateau at low $Wi_c < 1$. At high Wi_c, the shear-dependent Ψ_1 exhibit a power-law behavior with an exponent of approximately -1, independent of the arm length and the employed simulation method. Note that the power-law exponent becomes slightly larger for high c/c^* values in comparison with the solutions at low star concentrations; however, the differences in the exponents seem to be less pronounced than those for the viscosity curves in Fig. 10. We expect that in the asymptotic limit of large c/c^* the exponent approaches $-4/3$, as predicted by theory and observed for polymers.[24,43,50–54]

The corresponding normalized second normal-stress coefficients Ψ_2 are presented in Fig. 13 as a function of Wi_c. The values of Ψ_2 are noticeably noisier than the values of Ψ_1 and it is not fully clear if the zero-shear plateau can be reliably estimated from the simulation data. The power-law region at high Wi_c corresponds to the exponent of about -1.4 for all simulated N_m, close to the theoretically expected value for ψ_1. Finally, the simulated normal-stress coefficients agree very well for both, the MPC and DPD method.

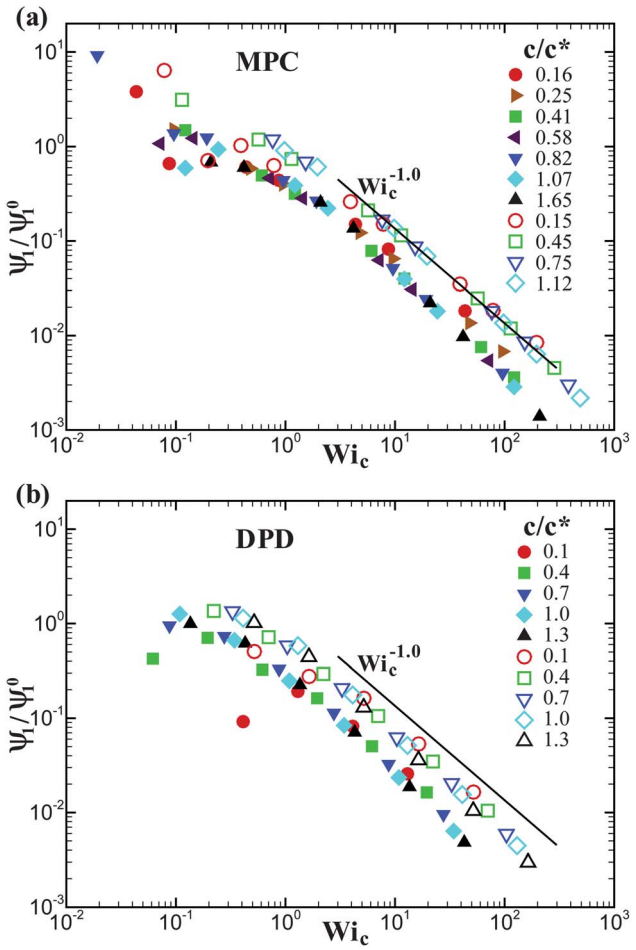

Fig. 12 First normal-stress coefficient Ψ_1, normalized by a concentration-dependent factor ψ_1^0 (see Fig. 14), as a function of Wi_c. (a) MPC simulation results, with arm lengths $N_m = 10$ (filled symbols) and $N_m = 30$ (open symbols), and various concentrations c/c^*, as indicated. (b) DPD simulation results for various star-polymer concentrations, as indicated, and $N_m = 10$ (filled symbols) and $N_m = 20$ (open symbols). The solid lines indicate a power-law dependence $\psi_1 \sim Wi_c^{-1}$; they are identical in (a) and (b).

The scale factors ψ_1^0 and ψ_2^0 normalized by $\eta_s^2 R_h^3/(k_B T)$ are shown in Fig. 14. These factors were obtained by scaling the normal-stress coefficients for various concentrations to the lowest available concentration for a given N_m. Under the assumption of a universal scaling of Ψ_1 and Ψ_2 for various concentrations, the factors ψ_1^0 and ψ_2^0 are proportional to the corresponding zero-shear-rate plateau values of the normal-stress coefficients. The factors ψ_1^0 and ψ_2^0 are rather similar for a given arm length, for both, the MPC and DPD calculations. Moreover, the MPC and DPD values agree very well for $N_m = 10$. The decrease of the values with increasing chain length is due to scaling by the hydrodynamic radius $R_h^3 \sim N_m^2$. The factors ψ_1^0, ψ_2^0 themselves exhibit a weak arm-length dependence only. The magnitude of the scale factors for both, the first and second normal-stress coefficients seem to be nearly identical, which points to a similar dependence of the zero-shear-rate plateau values on concentration for both Ψ_1 and Ψ_2.

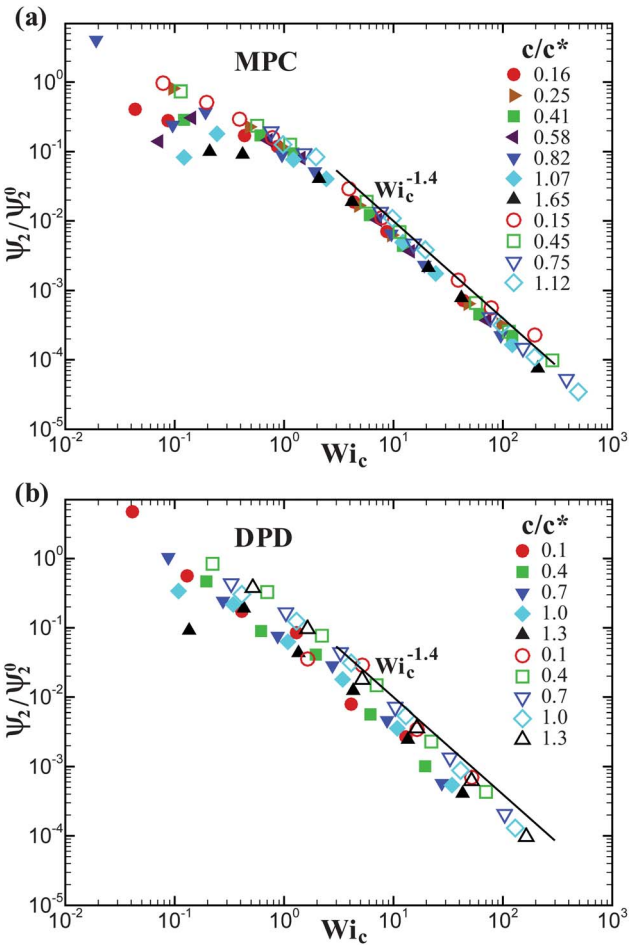

Fig. 13 Second normal-stress coefficient Ψ_2, normalized by a concentration-dependent factor ψ_2^0 (see Fig. 14), as a function of Wi_c. (a) MPC simulation results, with arm lengths $N_m = 10$ (filled symbols) and $N_m = 30$ (open symbols), and various concentrations c/c^*, as indicated. (b) DPD simulation results for various star-polymer concentrations, as indicated, and $N_m = 10$ (filled symbols) and $N_m = 20$ (open symbols).

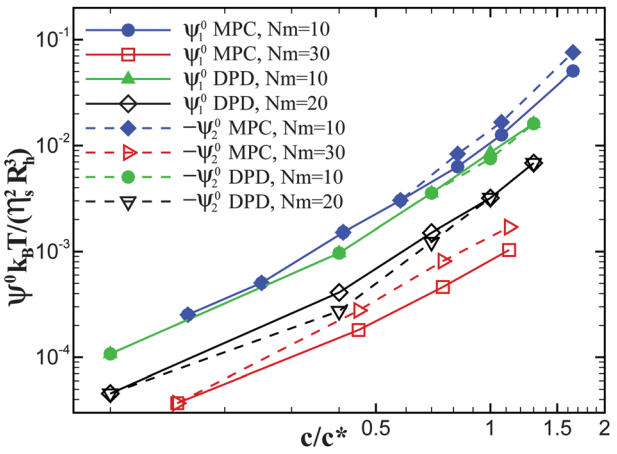

Fig. 14 Scaling factors ψ_1^0 and $-\psi_2^0$ (normalized by $\eta_s^2 R_h^3/(k_B T)$) for the normal-stress coefficients of star-polymer solutions for various concentrations. These factors are obtained by scaling the normal-stress coefficient curves for various concentrations (Fig. 12 and 13) to a reference curve, which corresponds to the lowest available concentration for a fixed N_m.

4 Summary and conclusions

We have investigated the flow behavior of dilute and semidilute solutions of star polymers in shear flow by two mesoscale hydrodynamics simulation techniques. The simulations show that many structural, dynamical, and rheological properties of star-polymer solutions can be described very well in terms of a concentration- and arm-length-dependent Weissenberg number $Wi_c = \dot{\gamma}\tau(c)$. This implies that the main effect of steric and hydrodynamic interactions on the star dynamics in dilute and semidilute solutions can be absorbed in the concentration- and arm-length-dependent relaxation time $\tau(c)$. Furthermore, we find that the behavior in the regime of small or large Weissenberg numbers is often well described by power laws, similar to those of semidilute solutions of linear polymers.[24]

An important aspect of our study is a detailed comparison of the predictions obtained by two frequently used particle-based hydrodynamics simulation techniques, MPC and DPD. As mentioned several times in Sec. 3, the agreement of the results for relaxation time, data collapse with concentration-dependent Weissenberg number, and power-law behavior is excellent. This is not self-evident, but requires that the parameters are chosen in the appropriate regime; here, it is particularly important to guarantee a sufficiently high Schmidt number (the ratio between momentum and mass transport). The good agreement between the two approaches strongly indicates that our results allow quantitative predictions and comparison with experimental results.

A careful look at corresponding figures for MPC and DPD reveals that there are small differences in the absolute values of several quantities. This can be seen most easily by comparing the simulation data to the lines indicating the power laws, because these lines are identical in corresponding figures. We attribute these differences mainly to small discrepancies in the star relaxation times of the two simulation approaches. We used the Zimm time to define a Weissenberg number, which appropriately captures the arm-length dependence, but is not necessarily identical to the relaxation time governing the dynamical properties of a star. Our simulation results suggest that the ratio of the Zimm time τ_z and the characteristic relaxation time of a star polymer is somewhat larger in MPC than in DPD simulations.

Scaling of conformational and dynamical properties of dilute and semidilute solutions with a concentration-dependent Weissenberg number Wi_c was obtained previously for *linear* polymers.[24] This raises the question about the similarities and differences in the flow behavior of linear and star-polymer solutions. Not unexpectedly, the qualitative behavior is similar in the two systems. It is also clear that the absolute values of deformation and orientation, viscosity and normal-stress coefficients are different. In general, star polymers seem to be less stretched and less aligned with the flow direction than linear polymers at a comparable Wi_c, and have a higher zero-shear viscosity—because stars resist stretching more than linear polymers due to the repulsive entropic and enthalpic interactions between their arms. Interestingly, similar power-law regimes are obtained for the various quantities for both, linear polymers and

star polymers of functionality $f = 10$. This suggests that the star properties are determined to a considerable extent by the polymer arms. To what extent the asymptotic behavior predicted for linear polymers is reached by the star-polymer systems remains to be investigated.

Finally, we can compare our simulation results with experimental studies of rheological properties.[15] The zero-shear viscosity increases more rapidly with concentration (with $\eta_0/\eta_s = 2.5\phi + 6.2\phi^2$) than for linear polymers[24] (where $\eta_0/\eta_s = 2.5\phi + 6.25k_H\phi^2$ with the Huggins coefficient[55,56] $k_H \simeq 0.3$), but less strongly than for hard-sphere colloids. Furthermore, the zero-shear viscosity as a function of c/c^* depends only very weakly on the arm length. A comparison of the experimental data for $f = 34$, $f = 62$, and $f = 124$ with the simulation results for $f = 10$ and $f = 2$ (linear polymers) is shown in Fig. 15. This shows a very consistent trend of an increase of the zero-shear viscosity with increasing functionality at constant concentration c/c^*, and demonstrates the crossover of star-polymer properties from ultra-soft to hard-sphere colloids with increasing functionality. A more detailed comparison requires simulations for larger functionalities and arm lengths.

The viscosity of star-polymer solutions of very high functionality $f \simeq 390$ has also been measured experimentally at concentrations in the fluid and glassy phases.[16] In the semidilute regime, the shear stress shows a linear increase at low shear rates, followed by a less pronounced growth with effective exponent of approximately 0.5; this effective exponent decreases with increasing concentration.[16] Both observations are consistent with our simulation results. The exponent of the power law of the shear stress for intermediate Weissenberg number is important, because a value larger than unity signals shear banding. Such a behavior has indeed been predicted for concentrated solutions.[22] On the basis of our simulations, no shear banding is predicted for $f = 10$ stars in the investigated concentration range. We expect that considerably larger functionalities are necessary to observe shear banding.

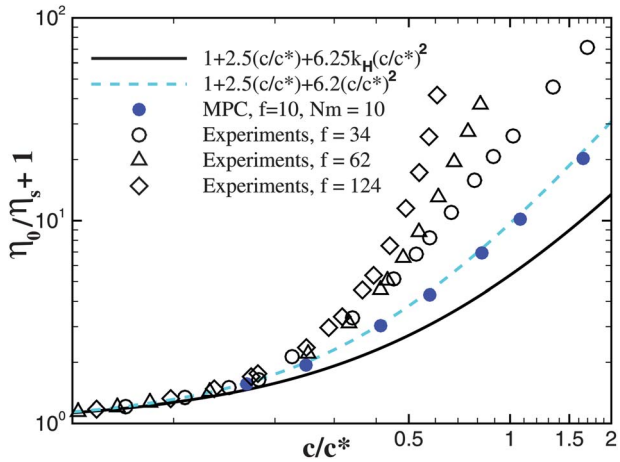

Fig. 15 Experimental and simulation results for the zero-shear viscosity of solutions of star polymers of different architecture. Experimental results (open symbols) for functionalities $f \geq 34$ are extracted from Fig. 6 of ref. 15. They are compared with the results for star polymers with $f = 10$ (closed symbols, dashed line) and for linear polymers (24) (solid line).

Acknowledgements

We thank J. K. G. Dhont, J. Stellbrink, D. Richter, M. Ripoll (Jülich), and D. Vlassopoulos (FORTH Crete) for stimulating discussions. Financial support by the Deutsche Forschungsgemeinschaft (DFG) through the Collaborative Research Center "Physics of Colloidal Dispersions in External Fields" (SFB TR6), and by the EU through the Collaborative Research Project "NanoDirect" (NMP4-SL-2008-213948) is gratefully acknowledged. D.A.F. acknowledges funding by the Humboldt Foundation through a postdoctoral fellowship.

References

1 R. G. Larson, *The Structure and Rheology of Complex Fluids*, Oxford University Press, New York, 1999.
2 D. Vlassopoulos and G. Fytas, *Adv. Polym. Sci.*, 2010, **236**, 1–54.
3 M. Daoud and J. P. Cotton, *J. Phys.*, 1982, **43**, 531.
4 C. N. Likos, H. Löwen, M. Watzlawek, B. Abbas, O. Jucknischke, J. Allgaier and D. Richter, *Phys. Rev. Lett.*, 1998, **80**, 4450–4453.
5 C. N. Likos, *Phys. Rep.*, 2001, **348**, 267–439.
6 T. M. Birshtein and E. B. Zhulina, *Polymer*, 1984, **25**, 1453.
7 T. M. Birshtein, E. B. Zhulina and O. V. Borisov, *Polymer*, 1986, **27**, 1078.
8 G. S. Grest, K. Kremer and T. A. Witten, *Macromolecules*, 1987, **20**, 1376.
9 M. Watzlawek, C. N. Likos and H. Löwen, *Phys. Rev. Lett.*, 1999, **82**, 5289–5292.
10 M. Laurati, J. Stellbrink, R. Lund, L. Willner, D. Richter and E. Zaccarelli, *Phys. Rev. Lett.*, 2005, **94**, 195504.
11 P. Ziherl and R. D. Kamien, *J. Phys. Chem. B*, 2001, **105**, 10147–10158.
12 G. M. Grason, B. A. DiDonna and R. D. Kamien, *Phys. Rev. Lett.*, 2003, **91**, 058304.
13 G. A. McConnell and A. P. Gast, *Macromolecules*, 1997, **30**, 435.
14 K. Ishizu, *Prog. Polym. Sci.*, 1998, **23**, 1383.
15 D. Vlassopoulos, G. Fytas, T. Pakula and J. Roovers, *J. Phys.: Condens. Matter*, 2001, **13**, R855–R876.
16 B. M. Erwin, M. Cloitre, M. Gauthierd and D. Vlassopoulos, *Soft Matter*, 2010, **6**, 2825–2833.
17 O. Ueberschär, C. Wagner, T. Stanger, C. Gutsche and F. Kremer, *Polymer*, 2011, **52**, 1829.
18 M. Ripoll, R. G. Winkler and G. Gompper, *Phys. Rev. Lett.*, 2006, **96**, 188302.
19 M. Ripoll, R. G. Winkler and G. Gompper, *Eur. Phys. J. E*, 2007, **23**, 349–354.
20 S. P. Singh, R. G. Winkler and G. Gompper, *Phys. Rev. Lett.*, 2011, **107**, 158301.
21 J. T. Padding, E. van Ruymbeke, D. Vlassopoulos and W. J. Briels, *Rheol. Acta*, 2010, **49**, 473–484.
22 W. J. Briels, D. Vlassopoulos, K. Kang and J. K. G. Dhont, *J. Chem. Phys.*, 2011, **134**, 124901.
23 W. J. Briels, *Soft Matter*, 2009, **5**, 4401–4411.
24 C.-C. Huang, R. G. Winkler, G. Sutmann and G. Gompper, *Macromolecules*, 2010, **43**, 10107–10116.
25 C.-C. Huang, G. Sutmann, G. Gompper and R. G. Winkler, *Europhys. Lett.*, 2011, **93**, 54004.
26 J. Hur, E. S. G. Shaqfeh, H. P. Babcock, D. E. Smith and S. Chu, *J. Rheol.*, 2001, **45**, 421.
27 A. Galuschko, L. Spirin, T. Kreer, A. Johner, C. Pastorino, J. Wittmer and J. Baschnagel, *Langmuir*, 2010, **26**, 6418.
28 A. Malevanets and R. Kapral, *J. Chem. Phys.*, 1999, **110**, 8605–8613.
29 R. Kapral, *Adv. Chem. Phys.*, 2008, **140**, 89.
30 G. Gompper, T. Ihle, D. M. Kroll and R. G. Winkler, *Adv. Polym. Sci.*, 2009, **221**, 1–87.
31 P. J. Hoogerbrugge and J. M. V. A. Koelman, *Europhys. Lett.*, 1992, **19**, 155–160.
32 P. Espanol and P. Warren, *Europhys. Lett.*, 1995, **30**, 191–196.
33 I. V. Pivkin, B. Caswell and G. E. Karniadakis, *Reviews in Computational Chemistry*, John Wiley & Sons, Inc., Hoboken, NJ, USA, 2010, vol. 27, pp. 85–110.

34 M. P. Allen and D. J. Tildesley, *Computer Simulation of Liquids*, Clarendon Press, Oxford, 1987.
35 A. Malevanets and J. M. Yeomans, *Europhys. Lett.*, 2000, **52**, 231.
36 M. Ripoll, K. Mussawisade, R. G. Winkler and G. Gompper, *Europhys. Lett.*, 2004, **68**, 106.
37 A. W. Lees and S. F. Edwards, *J. Phys. C: Solid State Phys.*, 1972, **5**, 1921–1928.
38 C.-C. Huang, A. Chatterji, G. Sutmann, G. Gompper and R. G. Winkler, *J. Comput. Phys.*, 2010, **229**, 168.
39 X. Fan, N. Phan-Thien, S. Chen, X. Wu and T. Y. Ng, *Phys. Fluids*, 2006, **18**, 063102.
40 D. A. Fedosov, I. V. Pivkin and G. E. Karniadakis, *J. Comput. Phys.*, 2008, **227**, 2540–2559.
41 C. M. Schroeder, R. E. Teixeira, E. S. G. Shaqfeh and S. Chu, *Phys. Rev. Lett.*, 2005, **95**, 018301.
42 C. Aust, M. Kröger and S. Hess, *Macromolecules*, 1999, **32**, 5660.
43 R. G. Winkler, *J. Chem. Phys.*, 2010, **133**, 164905.
44 J. H. Irving and J. G. Kirkwood, *J. Chem. Phys.*, 1950, **18**, 817–829.
45 R. G. Winkler and C.-C. Huang, *J. Chem. Phys.*, 2009, **130**, 074907.
46 D. A. Fedosov, G. E. Karniadakis and B. Caswell, *J. Chem. Phys.*, 2010, **132**, 144103.
47 A. Einstein, *Investigations on the theory of the Brownian movement*, Dover, New York, 1956.
48 G. K. Batchelor, *J. Fluid Mech.*, 1977, **83**, 97–117.
49 I. M. Krieger and T. J. Dougherty, *J. Rheol.*, 1959, **3**, 137–152.
50 A. V. Lyulin, D. B. Adolf and G. R. Davies, *J. Chem. Phys.*, 1999, **111**, 758.
51 D. Petera and M. Muthukumar, *J. Chem. Phys.*, 1999, **111**, 7614.
52 R. M. Jendrejack, J. J. de Pablo and M. D. Graham, *J. Chem. Phys.*, 2002, **116**, 7752.
53 C.-C. Hsieh and R. G. Larson, *J. Rheol.*, 2004, **48**, 995.
54 C. M. Schroeder, R. E. Teixeira, E. S. G. Shaqfeh and S. Chu, *Macromolecules*, 2005, **38**, 1967.
55 R. Pamies, J. G. Hernández Cifre, M. C. López Martínez and J. García de la Torre, *Colloid Polym. Sci.*, 2008, **286**, 1223.
56 Y. Takahashi, Y. Isono, I. Noda and M. Nagasawa, *Macromolecules*, 1985, **18**, 1002.

